




Cryo-EM structures of recombinant human sodium-potassium pump determined in three different states

Yingying Guo^{1,2,3,4}, Yuanyuan Zhang^{1,2,4}, Renhong Yan^{1,2,3,4} , Bangdong Huang^{1,2}, Fangfei Ye^{1,2}, Liushu Wu^{1,2}, Ximin Chi^{1,2} , Yi shi^{1,2} & Qiang Zhou^{1,2} ✉

Sodium-Potassium Pump (Na^+/K^+ -ATPase, NKA) is an ion pump that generates an electrochemical gradient of sodium and potassium ions across the plasma membrane by hydrolyzing ATP. During each Post-Albers cycle, NKA exchanges three cytoplasmic sodium ions for two extracellular potassium ions through alternating changes between the E1 and E2 states. Hitherto, several steps remained unknown during the complete working cycle of NKA. Here, we report cryo-electron microscopy (cryo-EM) structures of recombinant human NKA (hNKA) in three distinct states at 2.7–3.2 Å resolution, representing the E1·3Na and E1·3Na-ATP states with cytosolic gates open and the basic E2·[2K] state, respectively. This work provides the insights into the cytoplasmic Na^+ entrance pathway and the mechanism of cytoplasmic gate closure coupled with ATP hydrolysis, filling crucial gaps in the structural elucidation of the Post-Albers cycle of NKA.

¹Westlake Laboratory of Life Sciences and Biomedicine, Key Laboratory of Structural Biology of Zhejiang Province, School of Life Sciences, Westlake University, 18 Shilongshan Road, Hangzhou 310024 Zhejiang Province, China. ²Institute of Biology, Westlake Institute for Advanced Study, 18 Shilongshan Road, Hangzhou 310024 Zhejiang Province, China. ³Present address: Department of Biochemistry, School of Medicine, Southern University of Science and Technology, Shenzhen, Guangdong, China. ⁴These authors contributed equally: Yingying Guo, Yuanyuan Zhang, Renhong Yan. ✉email: zhouqiang@westlake.edu.cn

The sodium potassium pump (Na^+/K^+ -ATPase, NKA) is expressed in the plasma membrane of all animal cells and belongs to the P2-type ATPase family^{1–3}. NKA converts energy derived from ATP hydrolysis into an electrochemical potential gradient of Na^+ and K^+ across the plasma membrane, which is required for numerous physiological processes⁴. NKA undergoes an ATP-driven transport cycle called the Post-Albers scheme (Supplementary Fig. 1)^{5,6}, during which NKA exchanges three cytoplasmic Na^+ for two extracellular K^+ through transition between the E1 and E2 states coupled with hydrolysis of one ATP molecule. The E1 state of NKA has a higher affinity for Na^+ , while the E2 state has a higher affinity for K^+ .

NKA consists of a large multi-transmembrane catalytic α subunit, a single transmembrane β subunit, and an auxiliary γ subunit called FX_{YD}. There are four, three and seven isoforms for the α , β and γ subunits of human NKA (hNKA), respectively. The α subunit contains 10 transmembrane helices (M1–M10) and three cytosolic domains: the actuator (A) domain, the nucleotide-binding (N) domain, and the phosphorylation (P) domain. The A, N, and P domains of the α subunit form the cytoplasmic headpiece, which undergoes cycles of phosphorylation and dephosphorylation, resulting in closed and open conformation of the headpiece, respectively^{6,7}. The reported crystal structures of pig and shark NKA in the E2P·2K and E2·Pi·[2K] states with and without cardiotonic steroids provided valuable information for understanding the extracellular cation pathway^{8–12}. In contrast, only two structures in the E1 state (E1~P·[3Na]·ADP, Protein Data Bank (PDB) ID: 3WGU¹³ and 4HQJ¹⁴) have been reported, revealing an aspartyl-phosphorylated intermediate state with three cytoplasmic Na^+ occluded. NKA undergoes large conformational changes during K^+ release and Na^+ access to the ion-binding sites and is occluded by cytoplasmic gate closing. Therefore, questions about the cytoplasmic Na^+ entrance pathway and the gating mechanism on the cytoplasmic side have remained unanswered.

In this work, we report three cryo-electron microscopy (cryo-EM) structures of NKA in different states (E1·3Na, E1·3Na·ATP and E2·[2K]) of the Post-Albers cycle, which provides the structural insights into the cytoplasmic substrate entrance and the mechanism of cytoplasmic gating coupled with ATP hydrolysis, and improves the structural elucidation of the Post-Albers cycle of NKA.

Results

Structural determination of hNKA in three conformations. To solve the structures of hNKA and investigate its cytoplasmic gating mechanism, we overexpressed and purified hNKA that contained α 1, β 1 and γ 2 subunits (Supplementary Fig. 2a). To trap hNKA in the E1 state, only Na^+ and Mg^{2+} were added to the buffer during purification¹⁵. In the same way, the existence of only K^+ in solution can stabilize the conformation of hNKA in the E2 state¹⁵. We determined the cryo-EM structures of hNKA under three conditions: 1) 150 mM NaCl, 3 mM Mg^{2+} , 2) 150 mM NaCl, 3 mM Mg^{2+} , 1 mM ATP analogue adenosine 5'-O-(3-thio) triphosphate (ATP γ S), and 3) 100 mM KCl, 3 mM Mg^{2+} (Supplementary Figs. 2–4 and Supplementary Table 1). The cryo-EM structures solved under these conditions represent the E1·3Na, E1·3Na·ATP and E2·[2K] states at global resolution of 3.2 Å, 2.9 Å, and 2.7 Å, respectively, with higher local resolution in the transmembrane region. The map quality is good enough for model building except for some minor disordered regions. Some lipid-like densities were found near site A and site C¹⁶, for which the cholesterol analogue CHS and phosphatidic acid 3PH was manually built according to the purification conditions (Supplementary Fig. 5).

Overall structure of hNKA in E1 states. We successfully solved the cryo-EM structures of hNKA in the E1·3Na and E1·3Na·ATP states preceding ATP hydrolyzed at 3.2 Å and 2.9 Å resolution in the absence or presence of a slowly hydrolyzed ATP analogue (ATP γ S), respectively, which represent two E1 states of NKA preceding ATP hydrolysis previously unknown according to our knowledge (Fig. 1 and Fig. 2a, Supplementary Fig. 6a). Intriguingly, we observed an open pathway between the cytoplasm and Na^+ binding sites, resembling the Ca^{2+} pathway in the E1·ACP· Mg^{2+} (PDB ID:4H1W) state of SERCA¹⁷. The entrance of the open cytoplasmic cavity is located above the M1 kink and surrounded by M2, M3 and M4.

The structures of the E1·3Na and E1·3Na·ATP states are very similar to each other, with a root mean square deviation (RMSD) of 1.388 Å of 976 Ca atoms from a subunit, except for a slight difference in the Na^+ binding sites at the transmembrane region and in the ATP binding pocket at the cytoplasmic headpiece of the α 1 subunit (Fig. 2b–d, Fig. 3a–c and Supplementary Fig. 6b, 7a, 8a–c). In the E1·3Na and E1·3Na·ATP structures, NKA has three Na^+ binding sites, namely, I, II and III, which are surrounded by M4, M5, M6 and M8 (Fig. 2b–d). Compared with the E1~P·[3Na]·ADP state of pig NKA, sites I and II are different, whereas site III seems very conserved in those three E1 basic states (Fig. 2e; Supplementary Fig. 8c, d). It seems that during E1·3Na, E1·3Na·ATP to E1~P·[3Na]·ADP transition, ATP binding and hydrolysis affect Na^+ binding at sites I and II.

The E1·3Na and E1·3Na·ATP structures present two snapshots of the open conformation of the cytosolic headpiece without direct interaction between the A and N domains, which are significantly different from the E1~P·[3Na]·ADP state. The A domain is separated from the N domain and stabilized only by the eighth helix (Pa8) at the end of the P domain. However, in the E1~P·[3Na]·ADP state, the A domain interacts with the N domain through two additional sites, stabilizing the closed conformation of the headpiece¹³ (Supplementary Fig. 8e). Importantly, the movement and rotation of the A domain pull up the M1 helix after phosphorylation to close the cytoplasmic gate (Fig. 4a). However, in the Post-Albers cycle of SERCAa, a Ca^{2+} -ATPase, the cytosolic headpiece in the equivalent state E1·ACP· Ca^{2+} (PDB:1T5S)¹⁸ is patterned with a different closure conformation (Supplementary Fig. 12).

Na^+ -binding sites and an open cytoplasmic accessible pathway.

Since there are several nonprotein densities shown in two E1 cryo-EM maps at the mouth of the open accessible tunnel, we built the three most likely Na^+ locations by thorough analysis surrounding coordinating residues and comparison with the reported E1~P·[3Na]·ADP structure (Fig. 2 and Supplementary Fig. 7a Supplementary Tables 2 and 3). It seems that ion-binding sites I and III juxtaposed at M5, M6 and M8 are more reliable. Two residues, Ser782 on M5 and Asp815 on M6, are important for sites I and III formation. Site III is located between M5, M6 and M8 and the most restricted among three Na^+ binding sites (Fig. 2d–e, Supplementary Fig. 8a–d). The bulky side chain of Tyr778 on M5 forms a roof by cation- π interactions with site III Na^+ (Supplementary Fig. 7a). The Thr781, Thr814 and Gln930 residues are involved in Na^+ coordination at site III in the E1·3Na state, whereas the Asp933 residue is close to and coordinated with Na^+ in the E1·3Na·ATP state. Comparison between the E1·3Na and E1·3Na·ATP states shows that the binding of ATP causes a subtle shift of Na^+ at site I, which are coordinated with Ala330, Ser782, Asn783, Thr779 and Asp815 in the E1·3Na state and that are coordinated with Ala330, Ser782, Asn783, Glu786, Asp811 and a water molecule in the E1·3Na·ATP state.

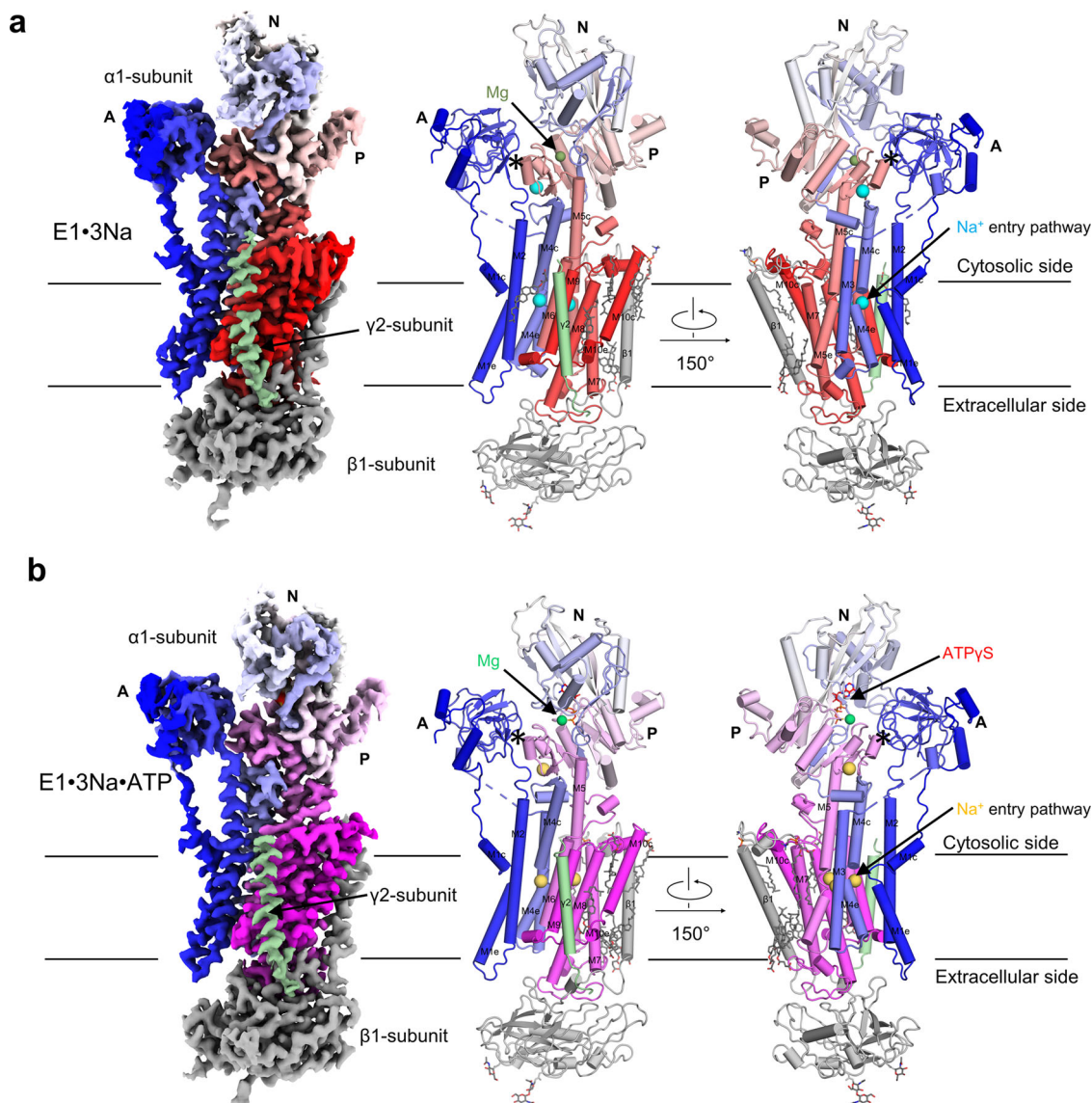


Fig. 1 Overall structures of NKA in the E1·3Na and E1·3Na·ATP states. a The overall cryo-EM map (left panel) and two views of the overall structure (middle and right panel) of the E1·3Na state. The $\alpha 1$ subunit is rainbow coloured from blue for the N-terminus to red for the C-terminus. $\beta 1$ subunit is coloured grey. $\gamma 2$ subunit is coloured pale green. **b** is the same as **(a)** but for the E1·3Na·ATP state (coloured as a spectrum from blue for the N-terminus to magenta for the C-terminus). Na^+ are coloured cyan or yellow in **(a)** or **(b)**, respectively. Mg^{2+} are coloured forest green or green in **(a)** or **(b)**, respectively. The glycosylation moieties are shown as sticks. e extracellular, c cytosolic, M transmembrane helix.

We calculated partial valence¹⁹ for Na^+ at sites I, II, and III in the E1·3Na state, which is 0.493, 0.397, and 0.653, respectively (Supplementary Table 2), indicating site III is a reasonable coordination site for a sodium ion. The relative lower valence values for site I, II (less than to 0.5²⁰) imply that sodium ion does not bind at these sites in a stable way. Whereas in the E1·3Na·ATP state, the partial valence for sites I, II, and III is 0.748, 0.313, and 0.717, respectively (Supplementary Table 3), increased at site I and III and decreased at site II.

The densities of Na^+ and the side chain of the gating residue Glu334 were not well resolved at site II in either E1·3Na or E1·3Na·ATP, while the density of other residues around the entrance of the cytoplasmic cavity was well resolved (Fig. 2b–d and Supplementary Fig. 7a). A possible Na^+ at site II according to surrounding coordinating residues Val329, Val332, Asp811 and waters was proposed. Glu334 has been reported as a gatekeeper that is highly conserved among P2-ATPases^{18,21,22} (Supplementary Fig. 13). Although previous studies have observed that

Glu334 is a part of site II for cation binding in the closed conformation¹⁸, we could not identify a stable conformation for the side chain of Glu334 due to weak density (Supplementary Figs. 4d, 7a). We speculate the side chain of Glu334 is unstable for the formation of Na^+ coordination. Large movement of site II Na^+ and the gating residue Glu334 was observed during the transition from the E1·3Na·ATP state to the E1~P·[3Na]·ADP state (Fig. 2e). Therefore, we speculate the gating residue Glu334 on M4, which has an unstable side chain, allows Na^+ entrance before the M1 sliding gate closure. Structural comparison between different E1 states shows that the Phe100 and Leu104 residues of hNKA (corresponding to residues Phe93 and Leu97 in pig NKA) are away from Glu334 in the E1·3Na·ATP state, allowing Glu334 to located in the open mouth of the entrance pathway of Na^+ (Supplementary Fig. 8a–d).

The binding mode of ATP γ S. P2-Type ATPase can be trapped in diverse stages of the Post-Albers catalytic scheme using ATP

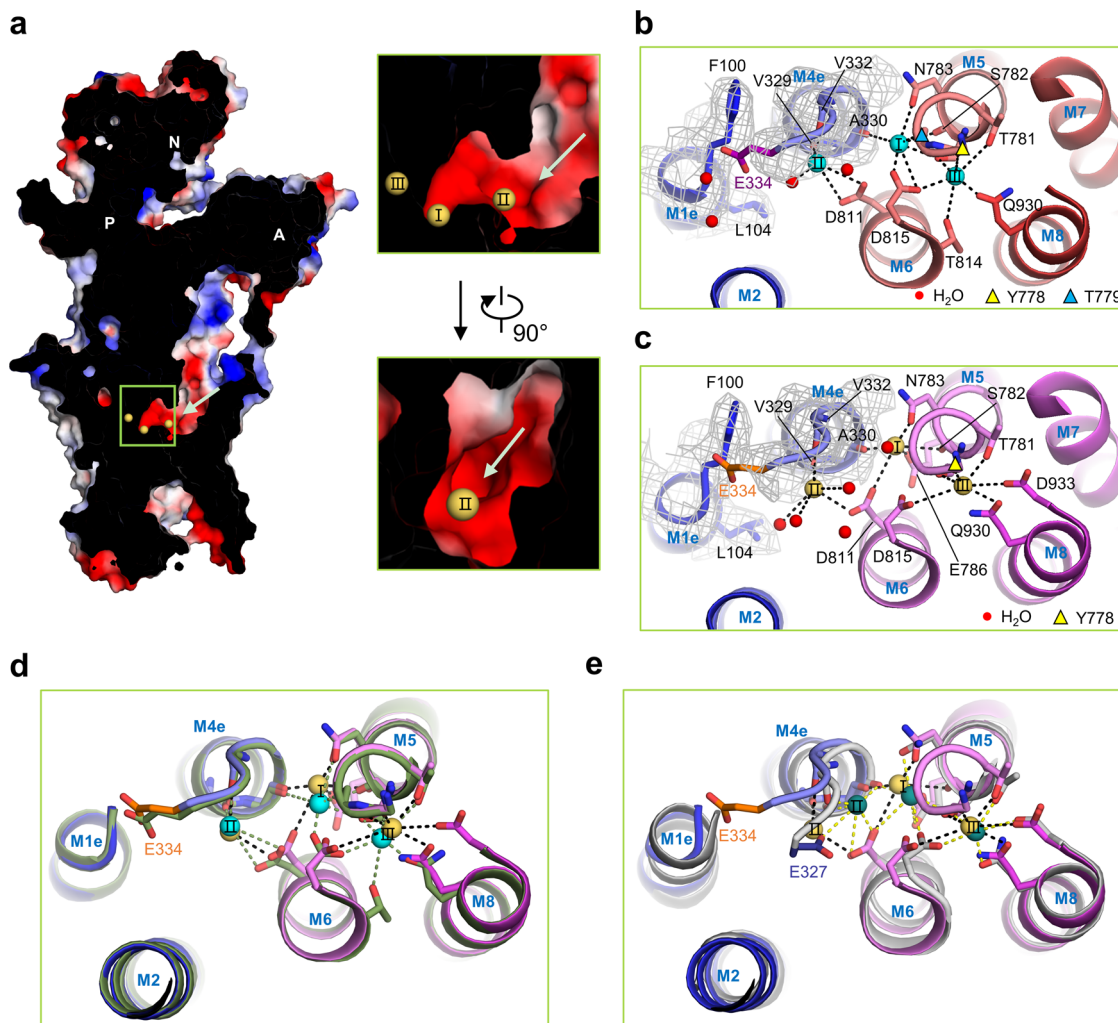


Fig. 2 Na^+ binding sites in different E1 states. **a** Cross-section through the Na^+ entry pathway in the E1-3Na-ATP state. Surface representation of the hNKA $\alpha 1$ subunit is coloured by vacuum electrostatics. Na^+ are coloured yellow. **b, c** are the transmembrane Na^+ binding sites in the E1-3Na and E1-3Na-ATP states, with Na^+ (labelled I, II and III) shown in cyan and yellow, respectively. The EM density around gate residue Glu334 are shown in grey mesh. The key residues coordinated with Na^+ within 4 Å are shown in sticks and indicated by dashed lines. The water molecules are shown as red balls. The yellow and blue triangles represent Tyr778 and Thr779 above the pictured field of view, respectively. **d** Binding mode comparison of Na^+ between the E1-3Na (dark green) and E1-3Na-ATP (spectrum from blue to magenta) states. **e** Binding mode comparison of Na^+ between the E1-3Na-ATP (spectrum from blue to magenta) and E1-P-[3Na]-ADP (grey) states. The gating residue Glu334 in human (Glu327 in pig) is coloured purple (E1-3Na), orange (E1-3Na-ATP), and slate (E1-P-[3Na]-ADP), respectively. Na^+ in E1-P-[3Na]-ADP are coloured deep teal. The structures in **(d)** and **(e)** are superimposed using M7-M10.

analogues, structural analogues of phosphorylation and different ionic conditions^{6,7}. In this study, ATP γ S was added to hNKA to mimic the ATP-bound E1 state instead of AMPPCP (ACP)^{18,23} or AMPPNP^{23,24} in SERCA.

In E1-3Na-ATP, the adenine ring of the bound nucleotide is stacked with Phe482 and interacts with Lys508 and Asp450 through π - π interaction, cation- π interaction, or hydrogen bond interaction (Fig. 3a). The ribose moiety is stabilized by Asp619 and Arg692, and the phosphate moiety interacts with Arg551 and Gly618 to maintain the kinked conformation of ATP γ S. The γ -phosphate of ATP γ S inserts into the P domain and is stabilized by the cofactor Mg^{2+} . The phospho-acceptor Asp376 in the highly conserved ³⁷⁶DKTG motif is primed to receive the γ -phosphate from ATP, while its side chain is oriented to Lys698 through a direct interaction, as in the E1-3Na state (Fig. 3b, c). Comparing ATP γ S with ADP and the stable phosphate analogue aluminium fluoride, we found that they adopt a similar binding mode (Fig. 4b). However, the orientation of the Asp376 side chain is

different from the upright conformation in E1-P-[3Na]-ADP (Fig. 3d). In addition, the terminal γ -phosphate of ACP in the E1-ACP-2Ca²⁺ state of SERCA¹⁸ interacts with the side chain of Asp351 (Asp376 in hNKA), which also shows an upright conformation resembling the case of E1-P-[3Na]-ADP (Supplementary Fig. 9a). The binding mode of ATP γ S in the E1-3Na-ATP state of hNKA is very similar to ACP in the E2-ACP state of SERCA2a, in which the Asp376 side chain faces Lys698 (Fig. 3e). We speculate that the reason for this difference is that ATP γ S binding can mimic a situation preceding NKA phosphorylation. As a result, ATP γ S is delivered to the phosphorylation site with a proper orientation to facilitate phosphoryl transfer.

Cytoplasmic gate closure coupled with ATP hydrolysis. Both the E1-3Na and E1-3Na-ATP states of hNKA have an open cytoplasmic pathway and an open headpiece (Supplementary Fig. 8). After ATP hydrolysis, the cytoplasmic gate is closed in

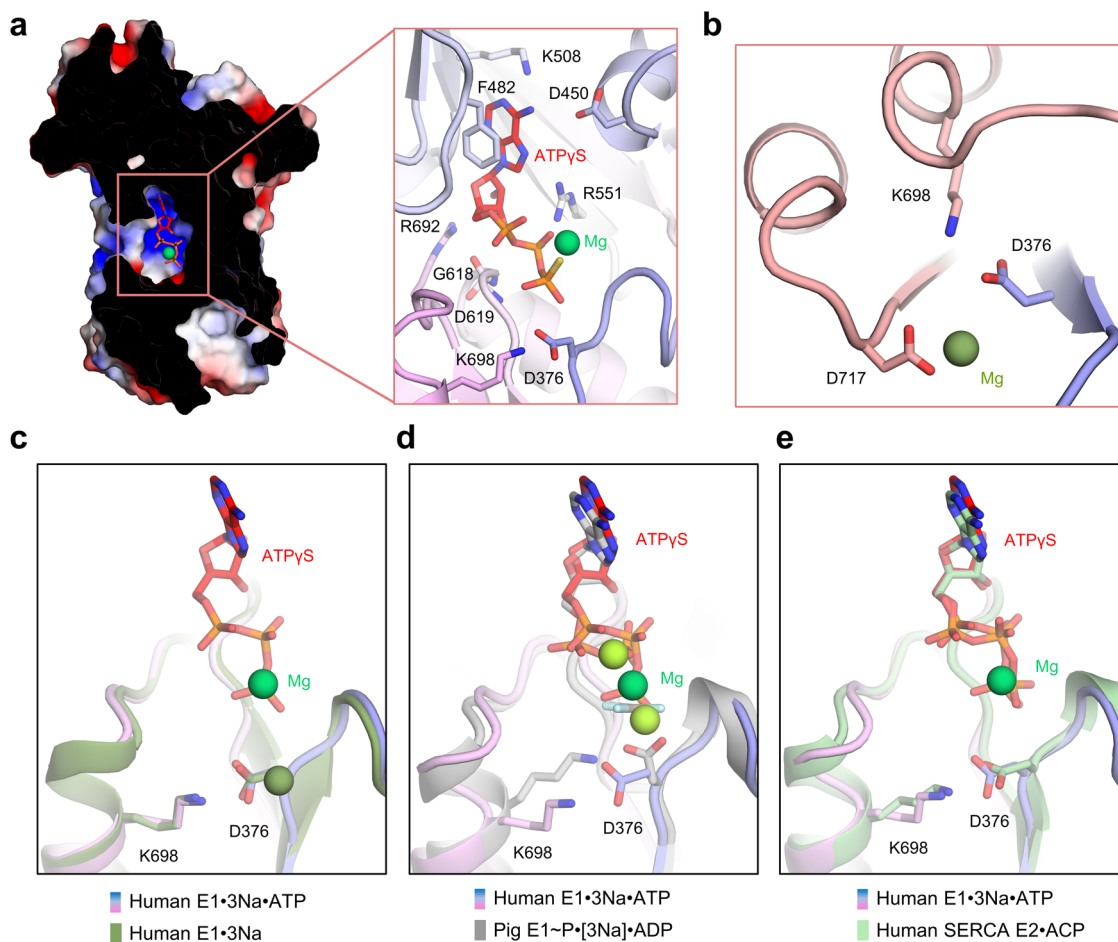


Fig. 3 ATP binding modes in NKA. **a** ATP binding pocket between the N and P domains and the key residues around ATP γ S (red). **b** Mg $^{2+}$ binding site and the phosphorylation site (Asp376) in the E1•3Na state. **c** Comparison of the Mg $^{2+}$ binding site and the phosphorylation site (Asp376) between the E1•3Na (dark green) and E1•3Na•ATP (blue to magenta) states. **d**, **e** Comparison of the ATP binding pocket between the E1•3Na•ATP (blue to magenta) and E1•P•[3Na]•ADP (grey) or SERCA E2•ACP (pale green) states. Mg $^{2+}$ are coloured forest green, green and pea green in E1•3Na, E1•3Na•ATP and E1•P•[3Na]•ADP, respectively.

the E1~P•[3Na]•ADP state, in which the cytosolic headpiece is also closed. ATP hydrolysis takes place in the cytosolic headpiece, spatially more than 50 Å distant to the Na $^{+}$ binding sites at the transmembrane region. It is important to know how ATP hydrolysis is coupled with the closure of cytoplasmic gate. The P domain of NKA have a Rossmann fold core, which contains a central parallel β -sheet with seven strands (P β 1–P β 7) and associated α -helices (P α 2–P α 7)²⁵. Comparison among three NKA E1 structures aligned to their N-terminal half of the P domain (P $_N$ domain, comprises P β 1–4) revealed that nucleotide binding induces rotation of the N domain with respect to the P domain using Arg692 in P $_N$ domain as a pivot point, which is on a short loop connecting the third strand (P β 3) and the sixth helix (P α 6) (Fig. 4b, Supplementary Fig. 9b, c). The ATP hydrolysis-coupled movement of the C-terminal half of the P domain (P $_C$ domain, comprises P β 5–P β 7) towards Asp376 changes the orientation of the Asp376 side chain (Fig. 3d) and the orientation of the A domain that sits on the P α 8 helix of the P domain (Fig. 4b, c). Finally, the movement of the N and A domains closes the cytosolic headpiece, pulls up the M1 helix after phosphorylation and closes the cytoplasmic gate (Fig. 4a).

K $^{+}$ -occluded E2 basic state. In addition to the E1•3Na and E1•3Na•ATP states described above, we also solved a cryo-EM structure of hNKA in the E2•[2K] state at 2.7 Å resolution, which is

in a ground occluded state bound with two K $^{+}$ following dephosphorylation (Fig. 5 and Supplementary Fig. 3b). A cytoplasmic K $^{+}$ site (site C) is the third K $^{+}$ binding site (Fig. 5a), which is implicated in the activation of dephosphorylation²⁶. Compared to the E2•[2K]•Pi state (a preceding state in the Post-Albers cycle)⁸, the two structures are very similar, with an RMSD of 1.083 Å between 994 Ca atom pairs of a subunit (Supplementary Fig. 10). The K $^{+}$ binding sites I and II between M4, M5 and M6 are almost identical (Fig. 5b and Supplementary Fig. 7b, 10c). The K $^{+}$ coordinating residues at site I (Asp811, Thr779, Ser782, Glu786 and Asn783) and site II (Asp811, Glu334, Val332, Val329, Ala330, Glu786 and Asn783) are similar to those at Na $^{+}$ binding sites I and II in the E1•3Na state (Supplementary Fig. 11). The ²¹⁹TGES motif of the A domain, which plays an important role in the dephosphorylation of E2P to E2 transition^{27–29}, is further stabilized by Mg $^{2+}$ and ³⁷⁶DKTG motifs in the P domain (Fig. 5c, d). Compared with the E1•3Na state, the α 1 subunit undergoes a large conformational change (Supplementary Fig. 11c). In the TM region, M1 to M6 rotate towards the opposite side by approximately 20°, whereas M7 to M10 are relatively rigid. When the P $_N$ domain is aligned, the N domain tilts 99°, and the A domain rotates approximately 71° relative to the E1•3Na state (Supplementary Fig. 11a). The ²¹⁹TGES motif is moved to expose the conserved Asp376 phosphorylation site during the transition from the E2•[2K] to E1•3Na state (Supplementary Fig. 11c).

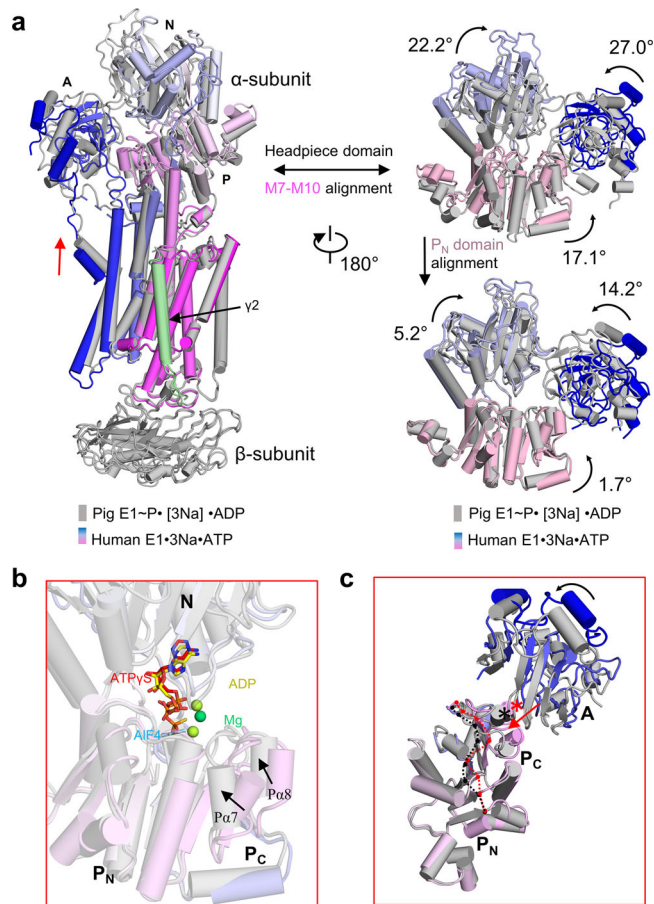


Fig. 4 P domain conformation change causes cytoplasmic gate closure.

a Structural comparison of the E1-3Na-ATP (blue to magenta) with E1-P-[3Na]-ADP (grey) states with the movement of the M1 helix and cytosolic headpiece shown. The structures are superimposed with M7-M10 or the P_N domain (598-710 residues). Red arrows represent closing of the M1 sliding door. **b, c** The structures are superimposed with the P_N domain (598-710 residues) between the E1-3Na-ATP and E1-P-[3Na]-ADP states. The ATP (red) and ADP (yellow) binding pockets between the N and P domains are shown in **(b)**. The P_N and P_C half domains have a bent conformation in the E1-3Na-ATP state (indicated by the red dashed line) or an unbent confirmation in the E1-P-[3Na]-ADP state (indicated by the black dashed line), respectively. The A domain sitting on a helix (Pa8) are denoted with asterisk in E1-3Na-ATP (red) and in E1-P-[3Na]-ADP (black). Red arrow indicates movement of Pa8 during transition from the E1-3Na-ATP state to the E1-P-[3Na]-ADP state.

Discussion

More than 30 crystal structures of NKA have been published, focusing mainly on three basic states (E1~P-[3Na]-ADP, E2P-2K and E2-Pi-[2K]) in the Post-Albers cycle. Here, we presented three cryo-EM structures of NKA in different states using recombinant proteins. To explore the state of our structures, we calculated the paired RMSD values of all NKA structures (Supplementary Fig. 14). The calculation results revealed that E1-3Na-ATP and E1-3Na in this work belong to the E1 state and are quite distinct from the E1~P-[3Na]-ADP state. Most of the pre-existing structures (85%) belong to the E2 state and can be classified into the E2-P and E2-Pi states. E2-[2K] in this work is more similar to the E2-Pi state than to the E2-P state. Therefore, our work has revealed three conformations representing different states in the Post-Albers cycle, for which no structural information has been reported before.

NKA used for crystallization was purified from an endogenous source, such as kidney or shark rectal glands. However, crystallization of NKA turned out to be particularly difficult³⁰, although recombinant proteins were already used to study the other P2-type members (SERCA³¹ and H⁺,K⁺-ATPase³²). Here, we develop a suitable strategy for structural determination using a heterologous expression system and pave the way for further investigation of the NKA complex that will likely be difficult for crystallography. Beyond this, the use of ATPγS to trap NKA in the E1 state suggest that ATPγS is an ATP analogue that can mimic a situation preceding NKA phosphorylation.

Our data provides the structural insights into the cytoplasmic ion-exchange pathway of NKA. We speculate that a gating mechanism takes place in the cytoplasm in two stages (Supplementary Fig. 15 and Supplementary Movie 1). The first stage is gate open towards the intracellular side during the transition from the E2-[2K] state to the E1-ATP state. Then, two K⁺ are released into the cytosol. At this time, the side chain of gating residue Glu334 is likely disordered, indicating that the cytoplasmic gate appeared to be open as a consequence of Glu334 disorder. Thus, three Na⁺ are able to bind from the intracellular side. It seems likely that sites I and II and the side chain of gating residue Glu334 near the door are unstable when Na⁺ binds to NKA according to EM density (Fig. 2 and Supplementary Fig. 7a) and Na⁺ valence (Supplementary table 2). The second gating stage at the cytoplasmic side is the gate closure during the transition from the E1-3Na-ATP state to the E1~P-[3Na]-ADP state (Fig. 4 and Supplementary Fig. 8). The M1 sliding door is elevated to close the cytoplasmic gate, accompanying the dramatically conformational changes with closed headpiece and an unbent P domain that was proposed in a recent publication about SERCA²⁵. The bending of the P domain is required for making phosphoryl transfer possible. Intriguingly, our data imply that ATPγS binding mode in hNKA is different from ACP in the SERCA E1-2Ca-ATP state^{18,33}, but is similar to ACP in the SERCA E2-ACP state²⁵ (Fig. 3 and Supplementary Fig. 9a). ACP in E1-2Ca-ATP is able to induce P_C domain in a similar unbent conformation as AlF₄⁻ and ADP do in NKA¹³. We found that Asp376 side chain has an upright orientation, which is likely induced by the interaction between γ phosphate of ATP and catalytic Asp376, is very important for the gate closure mechanism by causing the P_C domain bending releasing motion (Fig. 4b, c) by comparing ATPγS, ACP, and ADP binding pockets. This may be the reason for the M1 sliding door closed coupling NKA phosphorylation to Na⁺ binding site occlusion.

Methods

Protein expression and purification. The full-length cDNA of human α1 (Gene name: *ATP1A1*, GenBank accession number: BAA00061.1) was subcloned into pCAG with N-terminal FLAG tag, β1 (Gene name: *ATP1B1*, GenBank accession number: CAA27385.1) into pCAG with C-terminal Strep tag and no tag γ2 (Gene name: *FXYD2*, GenBank accession number: AAG37906.1) into pCAG vector. For protein expression, α1, β1 and γ2 were co-expressed in HEK 293F cells (Invitrogen) which were cultured in SMM 293T-II medium (Sino Biological Inc.) at 37 °C under 5% CO₂ in a Multitron-Pro shaker (Infors, 130 rpm). To transfect one liter of cells, 3 mg of polyethylenimines (PEIs) (Polysciences), 0.5 mg of the α1 plasmid, 0.5 mg of the β1 plasmid and 0.5 mg of the γ2 plasmid were preincubated with 50 mL fresh medium for 15 min and added into cell culture whose cell density reached 2.0 × 10⁶/mL. After 48 h of transfection, cells were harvested by centrifugation at 3800 × g for 10 min and resuspended in a buffer containing 25 mM Tris (pH 8.0), 3 mM MgCl₂ and 150 mM NaCl or 100 mM KCl for E1 or E2 state respectively, mixture of three protease inhibitors, aprotinin (1.3 μg/mL, AMRESCO), pepstatin (0.7 μg/mL, AMRESCO) and leupeptin (5 μg/mL, AMRESCO).

For protein purification, after incubating with 1.5% (w/v) n-dodecyl β-D-maltoside (DDM, Anatrace) supplemented with 0.1% (w/v) cholesteryl hemisuccinate tris salt (Anatrace) at 4 °C for 2 h, cells were centrifuged at 18,000 × g for 1 h to remove cell debris. The supernatant was loaded onto anti-FLAG M2 affinity resin (Sigma). The resin was washed with the wash buffer containing 25 mM Tris (pH 8.0), 3 mM MgCl₂, 150 mM NaCl or 100 mM KCl, 0.04% GDN (w/v), following by protein eluted with wash buffer plus 0.2 mg/mL

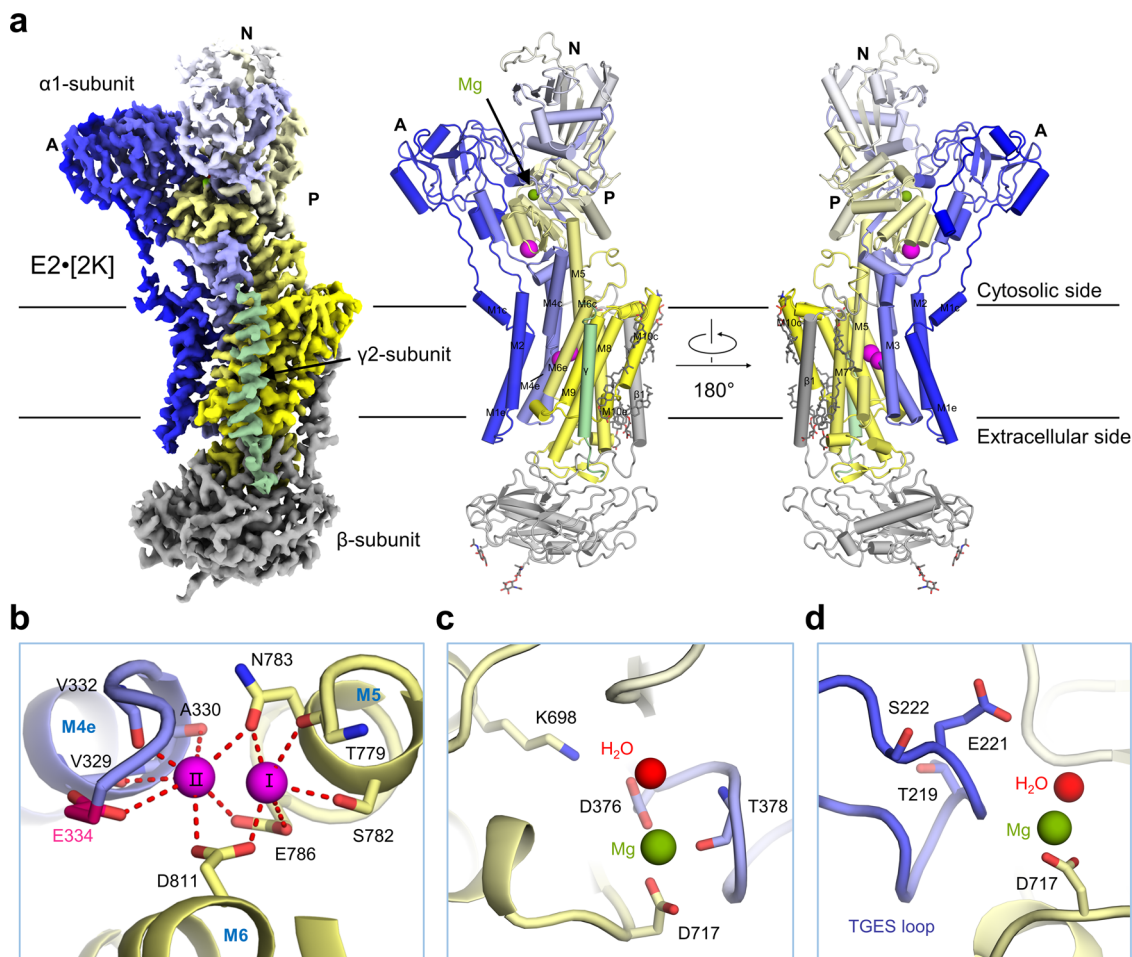


Fig. 5 Overall structure of E2-2[K]. **a** The overall cryo-EM map of E2-2[K] is shown in the left panel, and two perpendicular views of the overall structure are shown in the middle and right panels. The $\alpha 1$ subunit is rainbow coloured from blue for N-terminus to yellow for the C-terminus; the $\beta 1$ subunit is coloured grey; the $\gamma 2$ subunit is coloured pale green. **b** In the E2-2[K] state, two K^+ are bound to transmembrane K^+ binding sites (I and II). **c** Mg^{2+} stabilizes phosphorylation site (Asp376). **d** The hallmark TGES motif in the A domain is located near Mg^{2+} . K^+ are coloured magenta; Mg^{2+} is coloured olive green; and water molecules are coloured red. The glycosylation moieties are shown as sticks. e extracellular, c cytosolic, M transmembrane helix.

FLAG peptide. Then the protein complex was subjected to size-exclusion chromatography (Superose 6 Increase 10/300 GL, GE Healthcare) in buffer containing 25 mM Tris (pH 8.0), 3 mM $MgCl_2$, 150 mM NaCl or 100 mM KCl and 0.02% GDN. The peak fractions (14.5–15 ml) were collected and concentrated for EM analysis.

Cryo-EM sample preparation and data acquisition. The purified hNKA ($\alpha 1\beta 1\gamma 2$ complex) was concentrated to ~9 mg/mL and incubated with 1 mM ATP analogue (adenosine 5'-O-(3-thio) triphosphate, ATP γ S) in Na^+ buffer 1 h for E1-3Na-ATP state, absence of ATP γ S for E1-3Na and in K^+ buffer for E2-2[K] respectively, before being applied to the grids. Aliquots (3.3 μ L) of the protein complex were placed on glow-discharged holey carbon grids (Quantifoil Au R1.2/1.3). The grids were blotted for 3 s or 3.5 s and flash-frozen in liquid ethane cooled by liquid nitrogen with Vitrobot (Mark IV, Thermo Fisher Scientific). The cryo grids were transferred to a Titan Krios operating at 300 kV equipped with Gatan K3 Summit detector and GIF Quantum energy filter. Movie stacks were automatically collected using AutoEMation 2³⁴, with a slit width of 20 eV on the energy filter and a defocus range from -1.2 to -2.2 μ m in super-resolution mode at a nominal magnification of $\times 81,000$. Each stack was exposed for 2.56 s with an exposure time of 0.08 s per frame, resulting in a total of 32 frames per stack. The total dose rate was approximately 50 e-/ \AA^2 for each stack. The stacks were motion corrected with MotionCorr 2.1.1.0³⁵ and binned 2-fold, resulting in a pixel size of 1.087 \AA /pixel. Meanwhile, dose weighting was performed³⁶. The defocus values were estimated with Gctf 1.06³⁷.

Data processing. Particles were automatically picked from manually selected micrographs using Relion 3.0.6^{38–41}. After 2D classification, good particles were selected and generated an initial 3D reference, then subjected to the global angular searching 3D classification using the initial model with only one class. For each of the last several iterations of the global angular searching 3D classification, a local angular searching 3D classification was performed, during which the particles were

classified into 4 classes. Non-redundant good particles were selected from the local angular searching 3D classification. Then, these selected particles were subjected to multi-reference 3D classification, local defocus correction, 3D auto-refinement and post-processing.

The 2D classification, 3D classification and 3D auto-refinement were performed with Relion 3.0.6. The resolution was estimated with the gold-standard Fourier shell correlation 0.143 criterion⁴² with high-resolution noise substitution⁴³.

Model building and structure refinement. The atomic models of the hNKA were built based on the corresponding cryo-EM maps. A Chainsaw⁴⁴ model of the hNKA was first obtained using the previous structure of the sodium-potassium pump (PDB ID: 3KDP) as a template, which were further manually built in Coot 0.8.2⁴⁵. Each residue was manually checked with the chemical properties considered during model building. Structure real space refinement was performed with Phenix 1.14⁴⁶ with secondary structure and geometry restraints to prevent structure overfitting. To monitor the overfitting of the model, the model was refined against one of the two independent half maps from the gold-standard 3D refinement approach. Then, the refined model was tested against the other map. Statistics associated with data collection, 3D reconstruction and model refinement can be found in Table S1. Structure analysis and figures were performed or prepared with PyMOL 2.1.0 (www.schrodinger.com/pymol), Chimera 1.15⁴⁷ or ChimeraX 1.1⁴⁸.

Reporting summary. Further information on research design is available in the Nature Research Reporting Summary linked to this article.

Data availability

The data that support this study are available from the corresponding author upon reasonable request. The atomic coordinates and cryo-EM density maps of E1-3Na-ATP,

E1-3Na and E2-[2K] (PDB codes: 7E21 [<https://doi.org/10.2210/pdb7E21/pdb>], 7E1Z [<https://doi.org/10.2210/pdb7E1Z/pdb>] and 7E20 [<https://doi.org/10.2210/pdb7E20/pdb>]); whole maps: EMD-30949, EMD-30947 and EMD-30948 have been deposited in the Protein Data Bank and the Electron Microscopy Data Bank, respectively.

Received: 24 May 2021; Accepted: 24 June 2022;

Published online: 08 July 2022

References

- Palmgren, M. G. & Nissen, P. P-type ATPases. *Annu Rev. Biophys.* **40**, 243–266 (2011).
- Chan, H. et al. The p-type ATPase superfamily. *J. Mol. Microbiol. Biotechnol.* **19**, 5–104 (2010).
- Axelsen, K. B. & Palmgren, M. G. Evolution of substrate specificities in the P-type ATPase superfamily. *J. Mol. Evol.* **46**, 84–101 (1998).
- Jorgensen, P. L., Hakansson, K. O. & Karlsh, S. J. Structure and mechanism of Na,K-ATPase: functional sites and their interactions. *Annu Rev. Physiol.* **65**, 817–849 (2003).
- Post, R. L., Hegyvary, C. & Kume, S. Activation by adenosine triphosphate in the phosphorylation kinetics of sodium and potassium ion transport adenosine triphosphatase. *J. Biol. Chem.* **247**, 6530–6540 (1972).
- Dyla, M., Kjaergaard, M., Poulsen, H. & Nissen, P. Structure and mechanism of P-Type ATPase ion pumps. *Annu Rev. Biochem.* **89**, 583–603 (2020).
- Dyla, M., Basse Hansen, S., Nissen, P. & Kjaergaard, M. Structural dynamics of P-type ATPase ion pumps. *Biochem Soc. Trans.* **47**, 1247–1257 (2019).
- Morth, J. P. et al. Crystal structure of the sodium-potassium pump. *Nature* **450**, 1043–1049 (2007).
- Ogawa, H., Shinoda, T., Cornelius, F. & Toyoshima, C. Crystal structure of the sodium-potassium pump (Na⁺,K⁺-ATPase) with bound potassium and ouabain. *Proc. Natl Acad. Sci. USA* **106**, 13742–13747 (2009).
- Shinoda, T., Ogawa, H., Cornelius, F. & Toyoshima, C. Crystal structure of the sodium-potassium pump at 2.4 Å resolution. *Nature* **459**, 446–450 (2009).
- Laurson, M., Gregersen, J. L., Yatime, L., Nissen, P. & Fedosova, N. U. Structures and characterization of digoxin- and bufalin-bound Na⁺,K⁺-ATPase compared with the ouabain-bound complex. *Proc. Natl Acad. Sci. USA* **112**, 1755–1760 (2015).
- Kanai, R. et al. Binding of cardiotonic steroids to Na⁺,K⁺-ATPase in the E2P state. *Proc. Natl Acad. Sci. USA* **118**, e2020438118 (2021).
- Kanai, R., Ogawa, H., Vilsen, B., Cornelius, F. & Toyoshima, C. Crystal structure of a Na⁺-bound Na⁺,K⁺-ATPase preceding the E1P state. *Nature* **502**, 201–206 (2013).
- Nyblom, M. et al. Crystal structure of Na⁺, K⁺-ATPase in the Na⁺-bound state. *Science* **342**, 123–127 (2013).
- Jorgensen, P. L. Purification and characterization of (Na⁺, K⁺)-ATPase. V. Conformational changes in the enzyme Transitions between the Na-form and the K-form studied with tryptic digestion as a tool. *Biochim. Biophys. Acta* **401**, 399–415 (1975).
- Cornelius, F., Habeck, M., Kanai, R., Toyoshima, C. & Karlsh, S. J. General and specific lipid-protein interactions in Na,K-ATPase. *Biochim. Biophys. Acta* **1848**, 1729–1743 (2015).
- Winther, A. M. et al. The sarcolipin-bound calcium pump stabilizes calcium sites exposed to the cytoplasm. *Nature* **495**, 265–269 (2013).
- Sorensen, T. L., Moller, J. V. & Nissen, P. Phosphoryl transfer and calcium ion occlusion in the calcium pump. *Science* **304**, 1672–1675 (2004).
- Nayal, M. & Di Cera, E. Valence screening of water in protein crystals reveals potential Na⁺ binding sites. *J. Mol. Biol.* **256**, 228–234 (1996).
- Sauer, D. B. et al. Structure and inhibition mechanism of the human citrate transporter NaCT. *Nature* **591**, 157–161 (2021).
- Tsunekawa, N., Ogawa, H., Tsueda, J., Akiba, T. & Toyoshima, C. Mechanism of the E2 to E1 transition in Ca(2+) pump revealed by crystal structures of gating residue mutants. *Proc. Natl Acad. Sci. USA* **115**, 12722–12727 (2018).
- Clausen, J. D. et al. SERCA mutant E309Q binds two Ca(2+) ions but adopts a catalytically incompetent conformation. *EMBO J.* **32**, 3231–3243 (2013).
- Karlsen, J. L. & Bublitz, M. How to compare, analyze, and morph between crystal structures of different conformations: the P-Type ATPase example. *Methods Mol. Biol.* **1377**, 523–539 (2016).
- Olesen, C. et al. The structural basis of calcium transport by the calcium pump. *Nature* **450**, 1036–1042 (2007).
- Kabashima, Y., Ogawa, H., Nakajima, R. & Toyoshima, C. What ATP binding does to the Ca(2+) pump and how nonproductive phosphoryl transfer is prevented in the absence of Ca(2). *Proc. Natl Acad. Sci. USA* **117**, 18448–18458 (2020).
- Schack, V. R. et al. Identification and function of a cytoplasmic K⁺ site of the Na⁺, K⁺-ATPase. *J. Biol. Chem.* **283**, 27982–27990 (2008).
- Toyoshima, C. Structural aspects of ion pumping by Ca²⁺-ATPase of sarcoplasmic reticulum. *Arch. Biochem. Biophys.* **476**, 3–11 (2008).
- Anthonisen, A. N., Clausen, J. D. & Andersen, J. P. Mutational analysis of the conserved TGES loop of sarcoplasmic reticulum Ca²⁺-ATPase. *J. Biol. Chem.* **281**, 31572–31582 (2006).
- Clausen, J. D., Vilsen, B., McIntosh, D. B., Einholm, A. P. & Andersen, J. P. Glutamate-183 in the conserved TGES motif of domain A of sarcoplasmic reticulum Ca²⁺-ATPase assists in catalysis of E2/E2P partial reactions. *Proc. Natl Acad. Sci. USA* **101**, 2776–2781 (2004).
- Toyoshima, C., Kanai, R. & Cornelius, F. First crystal structures of Na⁺,K⁺-ATPase: new light on the oldest ion pump. *Structure* **19**, 1732–1738 (2011).
- Toyoshima, C. et al. Crystal structures of the calcium pump and sarcolipin in the Mg²⁺-bound E1 state. *Nature* **495**, 260–264 (2013).
- Abe, K., Yamamoto, K., Irie, K., Nishizawa, T. & Oshima, A. Gastric proton pump with two occluded K(+) engineered with sodium pump-mimetic mutations. *Nat. Commun.* **12**, 5709 (2021).
- Toyoshima, C. & Mizutani, T. Crystal structure of the calcium pump with a bound ATP analogue. *Nature* **430**, 529–535 (2004).
- Lei, J. & Frank, J. Automated acquisition of cryo-electron micrographs for single particle reconstruction on an FEI Tecnai electron microscope. *J. Struct. Biol.* **150**, 69–80 (2005).
- Zheng, S. Q. et al. MotionCor2: anisotropic correction of beam-induced motion for improved cryo-electron microscopy. *Nat. Methods* **14**, 331–332 (2017).
- Grant, T. & Grigorieff, N. Measuring the optimal exposure for single particle cryo-EM using a 2.6 Å reconstruction of rotavirus VP6. *Elife* **4**, e06980 (2015).
- Zhang, K. Gctf: Real-time CTF determination and correction. *J. Struct. Biol.* **193**, 1–12 (2016).
- Kimanius, D., Forsberg, B. O., Scheres, S. H. & Lindahl, E. Accelerated cryo-EM structure determination with parallelisation using GPUs in RELION-2. *Elife* **5**, e18722 (2016).
- Scheres, S. H. A Bayesian view on cryo-EM structure determination. *J. Mol. Biol.* **415**, 406–418 (2012).
- Scheres, S. H. RELION: implementation of a Bayesian approach to cryo-EM structure determination. *J. Struct. Biol.* **180**, 519–530 (2012).
- Scheres, S. H. Semi-automated selection of cryo-EM particles in RELION-1.3. *J. Struct. Biol.* **189**, 114–122 (2015).
- Rosenthal, P. B. & Henderson, R. Optimal determination of particle orientation, absolute hand, and contrast loss in single-particle electron cryomicroscopy. *J. Mol. Biol.* **333**, 721–745 (2003).
- Chen, S. et al. High-resolution noise substitution to measure overfitting and validate resolution in 3D structure determination by single particle electron cryomicroscopy. *Ultramicroscopy* **135**, 24–35 (2013).
- Winn, M. D. et al. Overview of the CCP4 suite and current developments. *Acta Crystallogr D. Biol. Crystallogr* **67**, 235–242 (2011).
- Emsley, P., Lohkamp, B., Scott, W. G. & Cowtan, K. Features and development of Coot. *Acta Crystallogr D. Biol. Crystallogr* **66**, 486–501 (2010).
- Adams, P. D. et al. PHENIX: a comprehensive Python-based system for macromolecular structure solution. *Acta Crystallogr D. Biol. Crystallogr* **66**, 213–221 (2010).
- Goddard, T. D. et al. UCSF ChimeraX: Meeting modern challenges in visualization and analysis. *Protein Sci.* **27**, 14–25 (2018).
- Goddard, T. D., Huang, C. C. & Ferrin, T. E. Visualizing density maps with UCSF Chimera. *J. Struct. Biol.* **157**, 281–287 (2007).

Acknowledgements

We thank the cryo-EM facility, the high-performance computing centre and the mass spectrometry & metabolomics core facility of Westlake University for providing the technical supports. This work was supported by the National Key R&D Program of China (2020YFA0509300) and the National Natural Science Foundation of China (projects 31800139, 31971123).

Author contributions

Q.Z. conceived the project. Q.Z. and Y.G. designed the experiments. Y.G., Y.Z. and R.Y. performed the experiments. F.Y., B.H., L.W. and X.C. contributed to the figures and movie. Y.S. contributed to the Na⁺ valence calculation. All of authors contributed to the data analysis. Q.Z. and Y.G. wrote the manuscript.

Competing interests

The authors declare no competing interests.

Additional information

Supplementary information The online version contains supplementary material available at <https://doi.org/10.1038/s41467-022-31602-y>.

Correspondence and requests for materials should be addressed to Qiang Zhou.

Peer review information *Nature Communications* thanks Kazuhiro Abe, Jens Morth and the other, anonymous, reviewer(s) for their contribution to the peer review of this work. Peer reviewer reports are available.

Reprints and permission information is available at <http://www.nature.com/reprints>

Publisher's note Springer Nature remains neutral with regard to jurisdictional claims in published maps and institutional affiliations.



Open Access This article is licensed under a Creative Commons Attribution 4.0 International License, which permits use, sharing, adaptation, distribution and reproduction in any medium or format, as long as you give appropriate credit to the original author(s) and the source, provide a link to the Creative Commons license, and indicate if changes were made. The images or other third party material in this article are included in the article's Creative Commons license, unless indicated otherwise in a credit line to the material. If material is not included in the article's Creative Commons license and your intended use is not permitted by statutory regulation or exceeds the permitted use, you will need to obtain permission directly from the copyright holder. To view a copy of this license, visit <http://creativecommons.org/licenses/by/4.0/>.

© The Author(s) 2022